

## Full Length Article

Prospects of annular differential phase contrast applied for optical sectioning in STEM<sup>☆</sup>Z. Lee<sup>\*</sup>, U. Kaiser, H. Rose

University of Ulm, Ulm 89081, Germany



## ARTICLE INFO

## Keywords:

Differential phase contrast  
STEMDepth of field  
Depth resolution

## ABSTRACT

The annular differential phase contrast (ADPC) mode in a third-order spherical aberration-corrected scanning transmission electron microscope (STEM) has recently been realized at an operating voltage of 300 kV by inserting a physical Fresnel phase plate in front of the objective lens and by using a detector geometry which matches that of the Fresnel phase plate [1]. By image calculation we explore the feasibility of this mode for the voltage range of 20–80 kV. Alternatively, we mimic the Fresnel phase plate material-free with the help of the adjustable aberrations of the corrector. The additional correction of chromatic aberration, fifth-order spherical aberration and image spread improves significantly the resolution and contrast. Under these advanced conditions it is possible to achieve optical sectioning in the ADPC mode with atomic resolution and a depth of field shorter than 3 Å for an accelerating voltage of 30 kV. Moreover, we show that the contrast obtained in the ADPC mode is clearly superior over the contrast in incoherent bright-field (IBF) and high-angle annular dark-field (HAADF), the two other common methods in STEM. We propose that with the advanced ADPC method applied in STEM, the investigation of the inner structure of thick samples will be possible without slicing.

## 1. Introduction

Scanning transmission electron microscopy (STEM) usually employs the high-angle annular dark-field (HAADF) mode for visualizing the atomic structure of objects. However, HAADF images show primarily heavy atoms because the contrast is approximately proportional to  $Z^2$ . Aberration correction offers the possibility to visualize low-Z atoms in the STEM by employing differential phase contrast (DPC) methods [2–5]. Two representative procedures are the annular differential phase contrast (ADPC) mode and the integrated differential phase contrast (IDPC) mode.

The ADPC mode uses a Fresnel phase plate, which is located at the front-focal plane of the objective lens. The phase plate can be realized either by adjusting the defocus and the correctable spherical aberrations appropriately [2,4] or by introducing a material phase plate [1]. The introduction of the Fresnel phase plate results in constructive and destructive interference patterns on the detector, and the interference patterns depend strongly on the geometry of the phase plate. The intensity resulting from the constructive and destructive interference is collected separately by the segments of a ring detector. The difference of these signals removes the nonlinear information and enhances the phase contrast [4]. This method was given the name MIDI-STEM [1], where MIDI stands for ‘matched illumination and detector

interferometry’. Considering that this method belongs to the DPC techniques, we decide to replace the name MIDI with ADPC, where A stands for annular, indicating that the geometry of the illumination and detector is different from the ones applied by other DPC techniques.

In the IDPC mode, the DPC images are first acquired by subtracting the signals collected by opposite segments of a quadrant detector [4]. By integrating the difference signals along the two symmetric axes of the segments, IDPC is obtained, demonstrating its advantage by suppressing high-frequency noise [4,6].

Besides these two procedures employing either a ring detector or a quadrant detector, other methods are proposed, which utilize different detector geometries and different algorithms for combining the signals of the detector elements. The proposed detector geometries comprise the bisectioned detector [3], the annular quadrant detector [7,8], the 16-segments detector [9] and the unitary detector [10]. Moreover, the pixelated detector is also used for DPC imaging since it can be used to generate any detector geometry with high efficiency and flexibility [11–13].

DPC methods in STEM have been used not only for visualizing low-Z materials [1,14], but have also been applied to investigate the magnetic structure [7,13,15], or the electronic structure [16–19] of the sample. An in-depth review of the DPC methods can be found in [20].

Among the different STEM–DPC techniques, we restrict our

<sup>☆</sup> Dedicated to Professor Jing Zhu on the occasion of her eighties birthday.

<sup>\*</sup> Corresponding author.

investigation to the ADPC method, which employs a Fresnel phase plate and a bright-field ring detector [1,2,4]. The development of the  $C_c/C_n$ -corrector ( $n=3, 5$ ) offers the possibility to fully utilize all differential phase contrast procedures [5]. Chromatic aberration is caused by the energy spread of the incident electrons, which reduces resolution and contrast of the STEM images especially at low accelerating voltages. Our theoretical investigations on the ADPC method are dedicated to a low-voltage STEM, which employs the  $C_c/C_n$ -corrector ( $n = 3, 5$ ) as a probe corrector [5,21]. We suggest a voltage range of 20–80 kV such as in the SALVE (sub-Angstrom low-voltage electron microscopy) instrument. The  $C_c/C_n$ -corrector ( $n = 3, 5$ ) provides the possibility to generate a material-free Fresnel phase plate by adjusting the spherical aberration coefficients and the defocus appropriately [4]. Combined with a pixelated detector matching the geometry of the Fresnel phase plate, the  $C_c/C_n$ -corrected STEM–DPC ( $n = 3, 5$ ) can achieve phase contrast with high flexibility and efficiency.

## 2. Method

The intensity pattern formed in the bright-field region of the STEM detector results from the interference of the elastically scattered wave with the non-scattered part of the incident wave. Optimum linear phase contrast is obtained in the aberration-corrected STEM by nullifying the chromatic aberration and by introducing a Fresnel phase plate. The Fresnel phase plate can be realized either by adjusting the spherical aberration coefficients  $C_n$ ,  $n = 3, 5, \dots$  and the defocus properly [4], or by employing a physical phase plate together with  $C_n = 0$  [1]. The phase plate must be designed in such a way that the areas of constructive and destructive interference are equal. Fig. 1 illustrates the method on the left and the plots on the right show the real part and the imaginary part of the transfer function  $T(\vec{q})$ , as well as the interference pattern in the detector plane. The interference pattern has been calculated by assuming that the probe is centred on a single atom. The calculations confirm that the structure of the interference pattern is strongly related to the structure of the phase of the incident wave. Maximum phase contrast is obtained by recording the areas of constructive and destructive interference with separate detectors, and by subtracting subsequently one signal from the other. A mathematical

derivation of the contrast obtained in the ADPC mode is given in Appendix A.

The contrast of weak phase objects is linearly related to the object potential in the ADPC mode. This behavior does not hold true for strong phase objects as outlined in Appendix A. For a weak phase object, the ADPC contrast can be expressed with a sufficient degree of accuracy by summing up the contributions of the individual atoms (A.12).

## 3. Influence of chromatic aberration and Johnson noise on the ADPC mode in STEM

In this section we will show the necessity to eliminate the chromatic aberration and to reduce the Johnson noise in order to successfully apply the suggested method. The effect of chromatic aberration on the contrast transfer function is taken into account by the mixed temporal coherence function:

$$E_c(\vec{q}, \vec{q}') = \exp\left[-\frac{1}{2}(\pi\sigma_c\lambda)^2(q^2 - q'^2)^2\right], \quad \sigma_c = C_c \frac{\sqrt{\langle(\Delta E)^2\rangle}}{E_0}. \quad (1)$$

The standard deviation of the chromatic focal spread  $\sigma_c$  depends on the coefficient  $C_c$  of the chromatic aberration, the mean quadratic energy spread  $\langle(\Delta E)^2\rangle$ , and the nominal electron energy  $E_0$ . The variables  $\vec{q}$  and  $\vec{q}'$  are 2D spatial frequency vectors, and  $\lambda = 2\pi/k$  is the wavelength of the electron.

As discovered recently, the image spread results from the Johnson noise, which is caused by the thermally induced currents in the lenses and in the elements of the corrector and the vacuum tube [22]. Image spread limits appreciably the attainable resolution and contrast in the  $C_c/C_n$ -corrected microscope ( $n = 3, 5$ ). The influence of the Johnson noise on the contrast transfer is described by the mixed image spread function  $E_{is}(\vec{q}, \vec{q}')$  [23]:

$$E_{is}(\vec{q}, \vec{q}') = \exp[-2(\pi\sigma_e)^2(\vec{q} - \vec{q}')^2]. \quad (2)$$

The standard deviation  $\sigma_e$  of the image spread depends on the voltage and is in the range between 20 pm and 30 pm for the SALVE microscope.

The contrast transfer function for the ADPC mode is given by

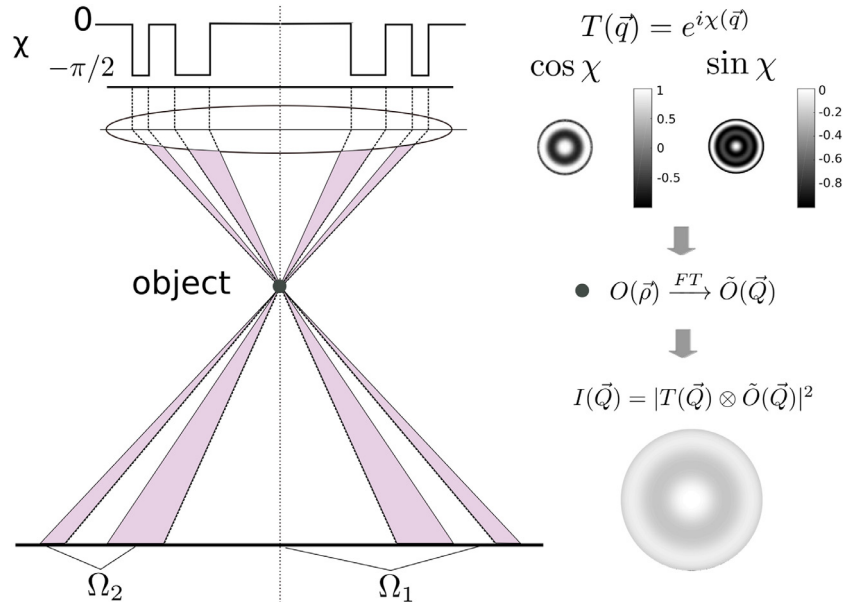


**Fig. 1.** Optimum differential phase contrast in the STEM requires a Fresnel phase plate, which must be designed in such a way that the area introducing a phase shift  $-\pi/2$  equals that introducing no phase shift. This ideal phase plate can be approximately realized by adjusting the coefficients  $C_n$  ( $n = 1, 3, 5$ ) appropriately. The simulations on the right illustrate the resulting phase transfer function  $T(\vec{q})$  structured by a  $C_c/C_3$ -aberration corrector. The interference pattern  $I(\vec{Q})$  shown on the bottom is obtained when the probe is centered on an atom.

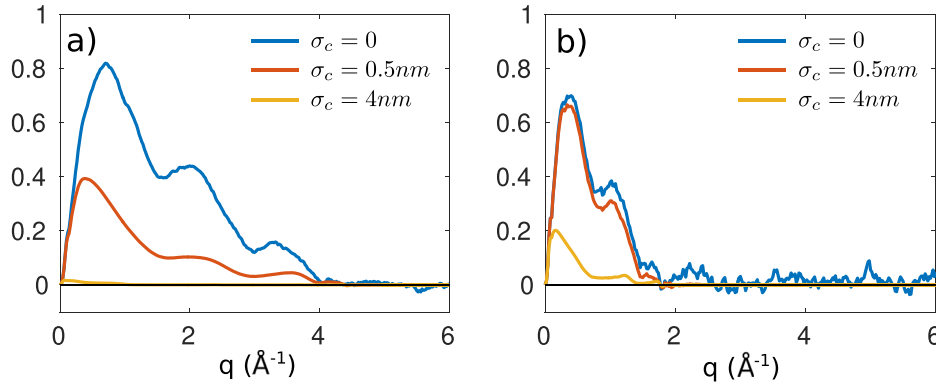


**Fig. 2.** Influence of focal spread on the ADPC transfer function  $T(\vec{q})$  for (a) the  $C_5$ -corrected STEM and (b) for the  $C_3$ -corrected STEM in the case of 30 kV. For the  $C_5$ -corrected STEM,  $C_7$  is set to 4 mm, and for the  $C_3$ -corrected STEM,  $C_5$  is set to 4 mm. Image spread has been neglected in both plots ( $\sigma_e = 0$ ).

$$T(\vec{q}) = i \int D(\vec{Q}) [T_{cc}(\vec{q} - \vec{Q}, -\vec{Q}) - T_{cc}(-\vec{q} - \vec{Q}, -\vec{Q})] d^2\vec{Q}. \quad (3)$$

Here  $\vec{Q}\lambda = \vec{\Theta}$  is the angular detector vector,  $D$  denotes the detector function. By including the mixed coherence functions  $E_c$  and  $E_{is}$ , the transmission cross coefficient is given by

$$T_{cc}(\vec{q} - \vec{Q}, -\vec{Q}) = A(\vec{q} - \vec{Q})A(-\vec{Q})\exp[-i\chi(\vec{q} - \vec{Q})]\exp[i\chi(-\vec{Q})] \\ \times E_{is}(\vec{q} - \vec{Q}, -\vec{Q})E_c(\vec{q} - \vec{Q}, -\vec{Q}). \quad (4)$$

Here,  $A$  and  $\chi$  denote the aperture function and the phase shift resulting from the geometrical aberrations, respectively.

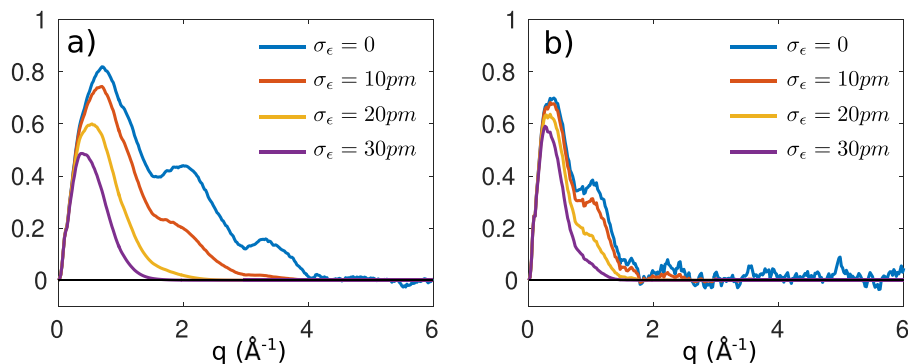
Fig. 2 shows the influence of chromatic aberration (characterized by focal spread (1)) on the contrast transfer functions for the ADPC mode in the  $C_5$ -corrected STEM (Fig. 2a) and for the  $C_3$ -corrected STEM (Fig. 2b). The influence of image spread has been neglected in both plots ( $\sigma_e = 0$ ). As can be seen, without focal spread ( $\sigma_c = 0$ ), the contrast transfer function is maximal, giving the highest contrast. As the focal spread increases to 4 nm in the case of the  $C_5$ -corrected STEM, the ADPC is totally damped, whereas in the case of the  $C_3$ -corrected STEM, a weak contrast transfer remains. This behavior indicates that the ADPC mode of the  $C_5$ -corrected STEM is more susceptible to the chromatic aberration than in the  $C_3$ -corrected STEM. Without  $C_c$ -correction,  $C_5$ -correction does not bring any benefit since the information limit is still determined by the chromatic aberration. Therefore, the ADPC mode operated in  $C_5$ -corrected STEM without  $C_c$ -correction performs even more poorly than in the  $C_3$ -corrected STEM.

Fig. 3 shows the influence of image spread on the contrast transfer functions for the  $C_c/C_5$ -corrected STEM (Fig. 3a) and for the  $C_c/C_3$ -corrected STEM (Fig. 3b). Without image spread ( $\sigma_e = 0$ ), the contrast transfer function gives the highest ADPC resolution, which is about 25 pm for the  $C_c/C_5$ -corrected STEM and 57 pm for the  $C_c/C_3$ -corrected

STEM. The impact of image spread on contrast and resolution of the ADPC mode is stronger for the  $C_c/C_5$ -corrected STEM than for the  $C_c/C_3$ -corrected STEM. For the  $C_c/C_5$ -corrected STEM, an image spread of  $\sigma_e = 30$  pm reduces ADPC resolution and contrast by about 50%, but not in the case of the  $C_c/C_3$ -corrected STEM. Therefore, the advantage of the ADPC mode for the  $C_c/C_5$ -corrected STEM compared with a  $C_c/C_3$ -corrected STEM can be demonstrated experimentally only if the image spread is largely reduced.

Figs. 2 and 3 illustrate that the ADPC mode is more susceptible to instabilities in a  $C_c/C_5$ -corrected STEM than in a  $C_c/C_3$ -corrected STEM, because chromatic aberration and image spread dampen the phase distribution of the corresponding phase plates differently. The total detector area covering the zones of zero phase shift must be equal to that covering the zones of phase shift  $-\pi/2$ . The limiting aperture angles of the ADPC mode calculated for the  $C_c/C_3$ -corrected and  $C_c/C_5$ -corrected STEM at 30 kV are 155 mrad and 63 mrad, respectively, using the parameters listed in Table 1. The chromatic aberration and the image spread affect the phase distribution of the phase plates differently for the two cases. In the case of the  $C_3$ -corrected STEM, the contrast transfer for large spatial frequencies is reduced, whereas it is nullified in the case of the  $C_5$ -corrected STEM. As a result, subtracting the intensity of the constructive interference from that of the destructive interference neither removes the non-linear background intensities, nor produces a high phase contrast.

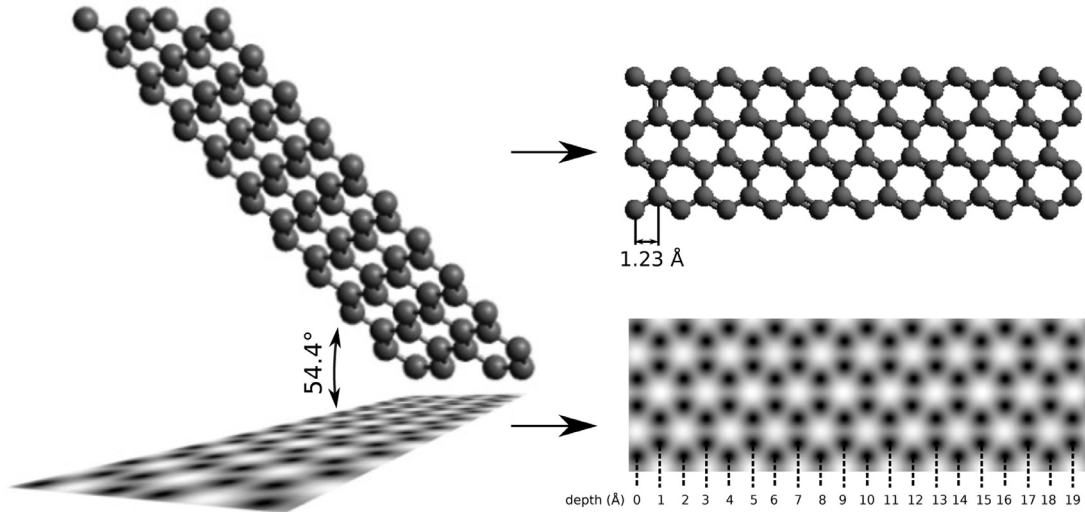
In summary, the correction of higher-order geometrical aberrations together with the elimination of chromatic aberration and Johnson noise is the prerequisite for the successful application of the ADPC mode in STEM. In the following we explore further the potential of the ADPC mode in the  $C_c/C_5$ -corrected STEM by assuming that these obstacles have been overcome.



**Fig. 3.** Influence of image spread on the ADPC transfer functions  $T(\vec{q})$  for (a) the  $C_c/C_5$ -corrected STEM and (b) for the  $C_c/C_3$ -corrected STEM at 30 kV. For the  $C_c/C_5$ -corrected STEM,  $C_7$  is set to 4 mm; and for the  $C_c/C_3$ -corrected STEM,  $C_5$  is set to 4 mm.

**Table 1**Parameters for the ADPC mode applied in the  $C_c/C_3$ -corrected STEM and the  $C_c/C_5$ -corrected STEM.

	$C_1$	$C_3$	$C_5$	$C_7$	$\theta_m$
$C_c/C_3$ -corr.	$\frac{9}{8}(6\lambda^2 C_5)^{1/3}$	$-(36\lambda C_5^2)^{1/3}$	fixed	none	$(\frac{36\lambda}{ C_5 })^{1/6}$
$C_c/C_5$ -corr.	$-\frac{C_7}{ C_7 }(108\lambda^3  C_7 )^{1/4}$	$5\frac{C_7}{ C_7 }(3\lambda  C_7 )^{1/2}$	$-\frac{C_7}{ C_7 }(972\lambda  C_7 ^3)^{1/4}$	fixed	$(\frac{192\lambda}{ C_7 })^{1/8}$

**Fig. 4.** Determination of the depth of field by imaging a tilted graphene slice. The slice is tilted by  $54.4^\circ$ , giving a projected distance between adjacent atom arrays of  $1.23\text{Å} \cdot \sin(54.4^\circ) = 1\text{Å}$ . The depth of field is obtained by counting the number of atom arrays in focus.

#### 4. Depth sensitivity of the ADPC imaging mode in STEM

On the condition that chromatic aberration is eliminated and Johnson noise is sufficiently reduced, large aperture angles can be employed in the ADPC mode, resulting in a high depth sensitivity. We verify this surmise by image simulation using a tilted slice of graphene.

Fig. 5 shows the image of a single layer of graphene tilted by  $54.4^\circ$  (Fig. 4). Since the distance between adjacent atom arrays is  $1.23\text{Å}$ , the vertical distance between adjacent atom arrays at this tilting angle corresponds to  $1\text{Å}$ . Based on the simulated focal series, with a focal range from 0 to  $10\text{Å}$  and a focal step of  $1\text{Å}$ , we immediately obtain the depth of field from a single simulated image by counting the number of atom arrays which are located within the depth of field. Here we define an atom array as the juxtaposition of the atoms along the vertical direction.

Fig. 5 shows focal series of ADPC images and incoherent bright-field (IBF) images of graphene tilted by  $54.4^\circ$  in the absence of chromatic aberration and image spread. The IBF images are obtained in the case of a uniform bright-field detector, whose maximum collection angle  $\theta_m$  coincides with the limiting aperture angle  $\theta_m$  of the scanning beam. The ADPC images of the  $C_c/C_5$ -corrected STEM show contrast reversal. By counting the number of atom arrays with dark contrast, we find  $3\text{Å}$  for the depth of field. The corresponding depth of field of the IBF mode is about  $4\text{Å}$ , which is only slightly less focus-sensitive than the ADPC mode. In the case of the  $C_c/C_3$ -corrected STEM, the depth of field is around  $18\text{Å}$  in the ADPC mode and  $\geq 20\text{Å}$  for the IBF mode.

The first column in Fig. 5 shows contrast reversal for the ADPC mode. In order to find the variation of the contrast with respect to the defocus, we have calculated the point spread function (PSF) for different defocus values, and plotted the central value  $I(0)$  of the PSF as a function of the deviation of the defocus from the optimum defocus  $df = 0$  (Fig. 6). The PSF is the Fourier transform of the CTF. The CTFs for optimum focus ( $df = 0$ ) are shown in Figs. 2 and 3 in the absence of focal spread and image spread ( $\sigma_c = 0$ ,  $\sigma_e = 0$ ). The positive and

negative values of  $I(0)$  in Fig. 6 represent bright and dark contrast of a point scatterer, respectively. The two curves are normalized based on the highest  $|I(0)|$  in each case. Fig. 6 demonstrates that the highest ADPC is obtained at optimum focus  $df = 0$  for both the  $C_c/C_5$ -corrected and the  $C_c/C_3$ -corrected STEM. With increasing deviation of the defocus from its optimum value  $df = 0$ , the contrast reverses its sign and then gradually vanishes. The ADPC varies faster with respect to defocus for the  $C_c/C_5$ -corrected STEM than for the  $C_c/C_3$ -corrected STEM. In the case of the  $C_c/C_5$ -corrected STEM, a defocus of  $df = \pm 10\text{Å}$  results in the highest opposite contrast, whereas in the case of the  $C_c/C_3$ -corrected STEM, maximum contrast reversal is obtained for  $df = -40\text{Å}$ . This behavior explains why the contrast reversal can be seen in the 1st column of Fig. 5, but not in the 3rd column; since the vertical distance of the tilted graphene slice is  $20\text{Å}$ , which is smaller than the  $40\text{Å}$  required to see the contrast reversal of the ADPC mode in the case of the  $C_c/C_3$ -corrected STEM.

The depth of field (DOF) is given by

$$DOF = \frac{\lambda}{\theta_m^2}. \quad (5)$$

Here  $\theta_m$  is the usable aperture angle listed in the caption of Fig. 5. In the case of the  $C_c/C_5$ -corrected STEM operating at  $30\text{ kV}$  with  $C_7 = 4\text{ mm}$ , we obtain a depth of field of  $2.9\text{Å}$  for the ADPC mode and  $4.1\text{Å}$  for the IBF mode. These results are close to our estimation obtained by counting the number of atom arrays based on Fig. 5. In the case of the  $C_c/C_3$ -corrected STEM, the depth of field is  $17.5\text{Å}$  in the ADPC mode and  $19\text{Å}$  in the IBF mode, which is also consistent with our estimation.

Fig. 7 shows the depth of field as a function of the accelerating voltage for different modes of the  $C_c/C_n$ -corrected STEM ( $n = 3, 5$ ). The figure shows that the depth of field for the ADPC mode is  $1\text{Å}$  shorter than that for the IBF and the HAADF modes. However, the values are only valid for weak phase objects because dynamic effects have been neglected.

In order to survey the influence of the dynamic effects, we consider



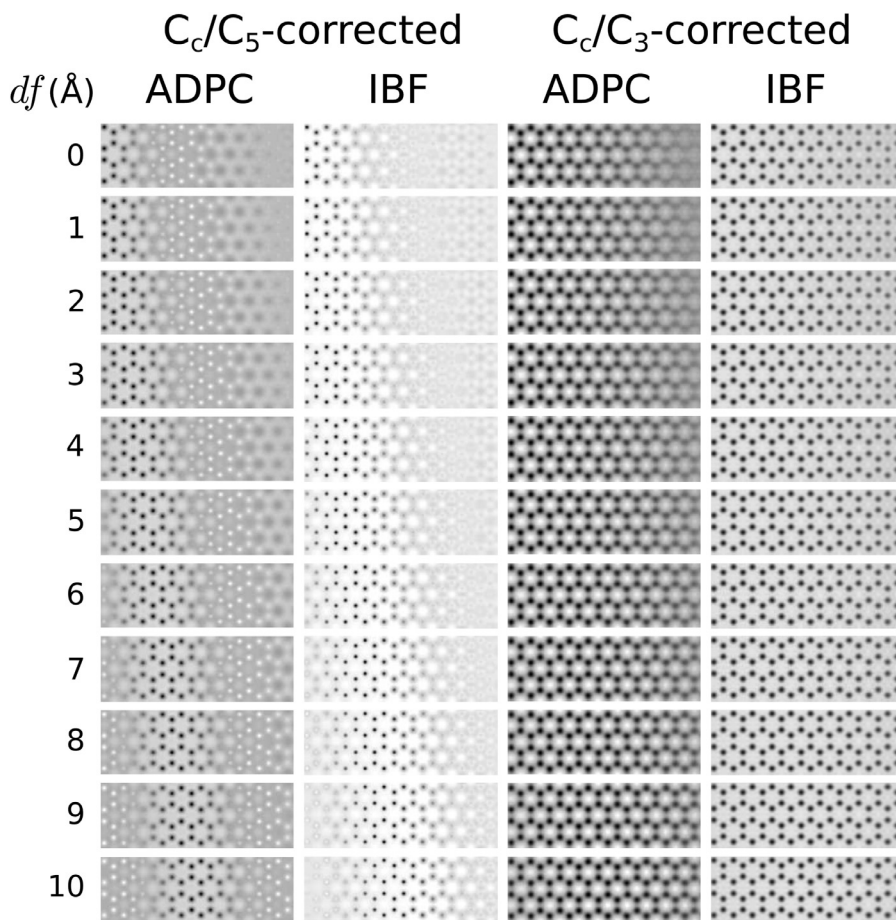


Fig. 5. Comparison of focal series images of tilted graphene (Fig. 4) between the ADPC mode and the IBF mode for a  $C_c/C_5$ -corrected STEM (left) and a  $C_c/C_3$ -corrected STEM (right) operated at 30 kV. The illumination aperture angles  $\theta_m$  are determined by using the formulas listed in Tables 1 and 2 and are (from left to right) 155 mrad, 130 mrad, 63 mrad and 60 mrad. The contrast of the IBF images is quite low compared with that of the ADPC images in this case. To illustrate the depth resolution of the IBF image clearly, the contrast of these images is intentionally maximized.

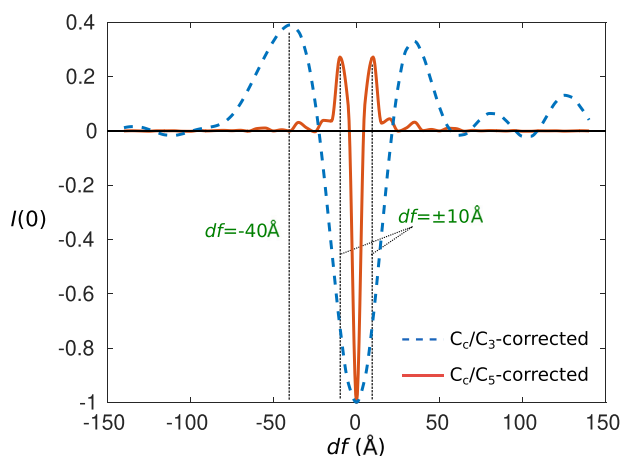


Fig. 6. Normalized central value  $I(0)$  of the point-spread function (PSF) of the ADPC mode for the  $C_c/C_5$ -corrected STEM and the  $C_c/C_3$ -corrected STEM operating at 30 kV. Positive and negative values of  $I(0)$  represent bright and dark contrast of the image of the point scatterer, respectively.

a 20 nm thick graphite sample for comparing the DOF of the ADPC, IBF and HAADF modes of a  $C_c/C_5$ -corrected STEM. The sample contains 62 atomic layers with an interlayer distance of 3.35 Å, which suffices to show dynamic effects at 30 kV. A germanium atom is substituted for a carbon atom in the 31th and 32th layers in the middle of the sample, as shown by the model in Fig. 8. By employing the multi-slice procedure, we have calculated a focal series of the IBF (1st column), HAADF (3rd column) and ADPC (2nd and 4th columns) images for this sample assuming an accelerating voltage of 30 kV,  $C_c = 0$  and correction of  $C_5$ . Since the contrast of an ADPC image depends on the order in which the

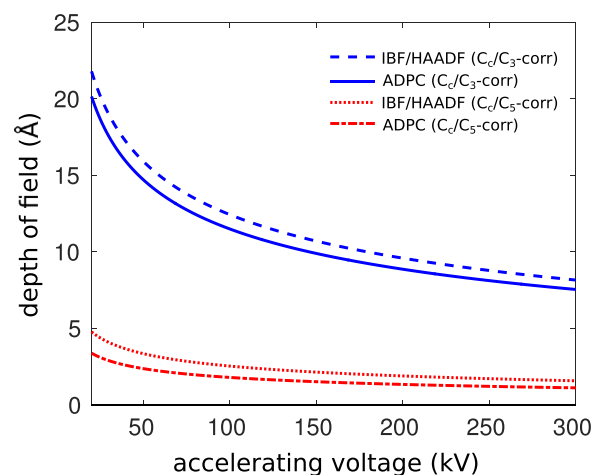
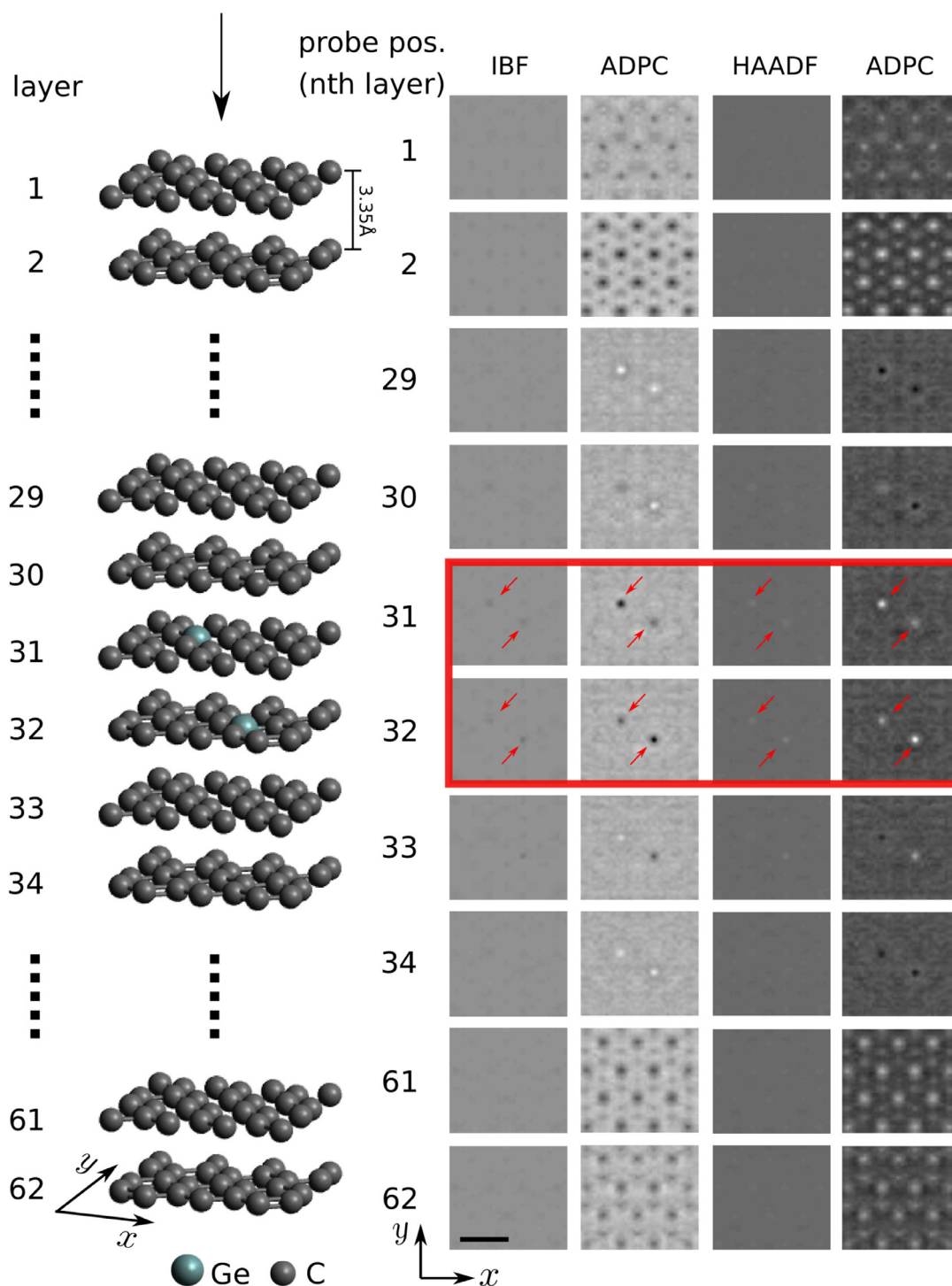


Fig. 7. Depth of field as a function of the accelerating voltage for the ADPC mode and the IBF and HAADF modes of a  $C_c/C_n$ -corrected STEM ( $n = 3, 5$ ). For the  $C_c/C_5$ -corrected STEM,  $C_7 = 4$  mm; and for the  $C_c/C_3$ -corrected STEM,  $C_5 = 4$  mm.

signals are subtracted, one obtains an ADPC image with bright-atom contrast simply by reversing the corresponding ADPC image with dark-atom contrast. The bright-atom contrast is suitable for comparing the ADPC mode and the HAADF mode. The 1st layer corresponds to  $df = 0$  and the focal step is set to 3.35 Å, so that at each defocus, the probe is positioned exactly at one of the layers. As the probe focuses at the 31th and 32th layer, respectively, a high-contrast image of the in-focus germanium atom shows up in the ADPC imaging mode, despite the dynamical scattering. In the cases of the IBF and the HAADF modes, the



**Fig. 8.** Focal series of simulated IBF, HAADF and ADPC images of a 20 nm thick graphite  $\langle 110 \rangle$  sample containing 62 atom layers, separated by 3.35 Å. In the 31th and the 32th layer, a germanium atom is substituted for a carbon atom. Spherical correction up to  $C_5$ , chromatic correction ( $C_c = 0$ ) and an accelerating voltage of 30 kV have been assumed. The ADPC images showing bright atoms are simply reversed from the corresponding ADPC images showing dark atoms. The collection angles are 0–130 mrad for the IBF images and 195–390 mrad for the HAADF images. Scale-bar: 0.5 nm.

contrast of the two germanium atoms is much weaker compared with the case in the ADPC mode. The images of these two atoms show up simultaneously with slightly different contrast. Although the depth resolution in the IBF and HAADF modes does not significantly deteriorate in the case of the 20 nm thick sample compared to the example of the tilted graphene (Fig. 5), the contrast in these two modes is much weaker than that in the ADPC mode. Moreover, due to the very low detection efficiency, the signal-to-noise ratio is much lower in the IBF and the

HAADF modes than in the ADPC mode for a given electron dose.

In summary, we can state that the depth resolution for all the three modes depends primarily on the usable aperture angle  $\theta_m$  given by the state of aberration correction. The larger the maximum illumination angle  $\theta_m$  is, the higher is the depth resolution. However, the signal-to-noise ratio for a given dose is much weaker in the IBF and HAADF modes than in the ADPC mode due to the low detection efficiency. For the  $C_c/C_5$ -corrected STEM, a large aperture angle  $\theta_m = 155$  mrad can

be obtained in the ADPC mode if the Johnson noise is sufficiently suppressed. This large aperture angle results in a short DOF of 2.9 Å at 30 kV, enabling the investigation of the inner structure of thick low-Z objects by optical sectioning.

## 5. Summary

We have illustrated the feasibility of the ADPC mode in the STEM at low accelerating voltages as low as 30 kV by simulations. We have shown the current limitations of the ADPC mode for the  $C_c/C_3$ -corrected STEM and the potential of this mode for an advanced  $C_c/C_5$ -corrected STEM. In addition to this improvement we demonstrated that image spread originating from thermal magnetic field noise needs to be eliminated or sufficiently suppressed in order to successfully realize the potential of the ADPC mode.

In order to show its potential for optical sectioning, we have shown by tilted graphene the dependence of the depth resolution on the state of geometrical and chromatic aberration correction. The ADPC mode in

an advanced  $C_c/C_5$ -corrected STEM provides a depth of field of 2.9 Å at 30 kV. Our example of a 20 nm thick graphite sample with two embedded Ge atoms substituting two C atoms imaged with the ADPC mode on a  $C_c/C_5$ -corrected STEM at 30 kV shows sharp contrast of the Ge atoms when the probe focuses at the corresponding depth. This result demonstrates that the ADPC method is applicable, even when dynamical scattering is present. Therefore we suppose that this mode will allow one to image the inner structure of relatively thick samples without slicing.

## Acknowledgments

We thank Michael Mohn for helpful discussions and gratefully acknowledge financial support by the DFG (German Research Foundation) and by the Ministry of Science, Research and the Arts (MWK) of the state Baden–Württemberg within the frame of the Sub-Angstrom Low-Voltage Electron microscopy (SALVE) Project (Grant No. KA 1295-10/3).

## Appendix A. Contrast obtained by the ADPC method

In order to find the relation between the contrast and the atomic potential of a phase object, it suffices to calculate the ADPC image of a single atom. The wave function  $\Psi(\vec{\rho})$  at the object plane  $z_0$  is given by

$$\Psi(\vec{\rho}) = FT[\Psi_0 T(\vec{q})]. \quad (\text{A.1})$$

Here  $\Psi_0$  is the incident plane wave and  $T(\vec{q})$  is the transfer function of the objective lens. The illumination for ADPC method is designed in such a way that within the solid angle  $\Omega_1$  no phase shift is introduced, whereas a phase shift of  $-\pi/2$  is introduced within the solid angle  $\Omega_2$ , as shown in Fig. 1. In this case, the transfer function  $T(\vec{q})$  satisfies the relation:

$$T(\vec{q}) = \begin{cases} 1, & \text{if } \vec{q} \in \vec{k} \Omega_1, \\ -i, & \text{if } \vec{q} \in \vec{k} \Omega_2. \end{cases} \quad (\text{A.2})$$

The interaction of the probe with an atom located at position  $\vec{\rho}_0$  is given by the product of the probe function and the object transmission function  $O(\vec{\rho})$ :  $\Psi(\vec{\rho} - \vec{\rho}_0)O(\vec{\rho})$ . The pattern recorded by the detector is therefore

$$\begin{aligned} I(\vec{Q}, \vec{\rho}_0) &= \left| \iint T(\vec{q}) O(\vec{\rho}) e^{-i\vec{\rho} \cdot (\vec{Q} - \vec{q})} e^{-i\vec{\rho}_0 \cdot \vec{q}} d^2\vec{\rho} d^2\vec{q} \right|^2 \\ &= \left| \int T(\vec{q}) \tilde{O}(\vec{Q} - \vec{q}) e^{-i\vec{\rho}_0 \cdot \vec{q}} d^2\vec{q} \right|^2 \\ &= |T_{\vec{\rho}_0}(\vec{Q}) \otimes \tilde{O}(\vec{Q})|^2, \end{aligned} \quad (\text{A.3})$$

where  $T_{\vec{\rho}_0}(\vec{Q}) = T(\vec{Q})e^{-i\vec{\rho}_0 \cdot \vec{Q}}$ . The relation (A.3) shows that the interference pattern recorded by the detector is the squared modulus of the convolution between the transfer function and the object spectrum.

Within the solid angle  $\Omega_1$  where no phase shift is introduced to the illumination, constructive interference takes place and the ring detector  $D_1(\vec{Q})$  is assigned to record the intensities of this region. Within the solid angle  $\Omega_2$  where a phase shift of  $-\pi/2$  is introduced to the illumination, destructive interference takes place and the ring detector  $D_2(\vec{Q})$  is assigned to record the intensities of this region. With this arrangement, the geometries of both illumination and detector match each other.

The two detector functions satisfy the following relations:

$$D_1(\vec{Q}) = \begin{cases} 1, & \text{if } \vec{Q} \in \vec{k} \Omega_1, \\ 0, & \text{otherwise.} \end{cases}, \quad D_2(\vec{Q}) = \begin{cases} 1, & \text{if } \vec{Q} \in \vec{k} \Omega_2, \\ 0, & \text{otherwise.} \end{cases} \quad (\text{A.4})$$

The area covered by  $D_1$  is equal to that covered by  $D_2$ :

$$\int D_1(\vec{Q}) d^2\vec{Q} = \int D_2(\vec{Q}) d^2\vec{Q}. \quad (\text{A.5})$$

The final image is formed by the difference signal recorded by  $D_1$  and  $D_2$ :

$$I(\vec{\rho}_0) = \int D_1(\vec{Q}) I(\vec{Q}, \vec{\rho}_0) d^2\vec{Q} - \int D_2(\vec{Q}) I(\vec{Q}, \vec{\rho}_0) d^2\vec{Q}. \quad (\text{A.6})$$

Noticing the relation between (A.2) and (A.4), we write  $T(\vec{Q})$  in (A.3) as

$$T(\vec{Q}) = D_1(\vec{Q}) - iD_2(\vec{Q}). \quad (\text{A.7})$$

For a phase object, the function  $O(\vec{\rho})$  can be written as the sum of its real and imaginary parts:

$$O(\vec{\rho}) = \exp[i\Phi(\vec{\rho})] = \cos(\Phi(\vec{\rho})) + i \sin(\Phi(\vec{\rho})). \quad (\text{A.8})$$

For a single atom,  $\cos(\Phi(\vec{\rho}))$  and  $\sin(\Phi(\vec{\rho}))$  are both real-valued even functions. Therefore, the Fourier transforms  $C(\vec{Q}) = FT[\cos(\Phi(\vec{\rho}))]$  and

**Table 2**

Parameters for the IBF and HAADF modes applied in the  $C_c/C_3$ -corrected STEM and the  $C_c/C_5$ -corrected STEM. The parameters are derived for positive  $C_5$  in the case of the  $C_c/C_3$ -corrected microscope and for positive  $C_7$  in the case of the  $C_c/C_5$ -corrected microscope.

	$C_1$	$C_3$	$C_5$	$C_7$	$\theta_m$
$C_c/C_3$ -corr.	$1.8627(C_3\lambda^2)^{1/3}$	$-3.041(C_3^2\lambda)^{1/3}$	Fixed	None	$1.7473(\frac{\lambda}{C_5})^{1/6}$
$C_c/C_5$ -corr.	$1.0314(C_7\lambda^3)^{1/4}$	$0.5289(C_7\lambda)^{1/2}$	$-2.5606(C_7^3\lambda)^{1/4}$	Fixed	$1.6243(\frac{\lambda}{C_7})^{1/8}$

$S(\vec{Q}) = FT[\sin(\Phi(\vec{\rho}))]$  are also real-valued even functions with respect to  $\vec{\rho}$ . Using these Fourier transforms we obtain

$$\tilde{O}(\vec{Q}) = FT[O(\vec{\rho})] = C(\vec{Q}) + iS(\vec{Q}). \quad (\text{A.9})$$

After calculating the detector pattern by inserting (A.7) and (A.9) into (A.3), we further obtain the difference signal by applying (A.6). As a result, the final ADPC image for a single atom is approximately

$$I(\vec{\rho}_0) \approx 4 \int S(\vec{Q}) \cos(\vec{\rho}_0 \cdot \vec{Q}) [D_1(\vec{Q}) \otimes D_2(\vec{Q})] d^2\vec{Q}. \quad (\text{A.10})$$

The relation (A.10) shows that the ADPC image of a single atom is only related to the imaginary part  $S(\vec{Q})$  of the object transmission function and the position of the scanning probe  $\vec{\rho}_0$ . For a weak phase object ( $O(\vec{\rho}) \approx 1 + i\Phi(\vec{\rho})$ ), the function  $S(\vec{Q}) \approx FT[\Phi(\vec{\rho})]$  can be approximated with a sufficient degree of accuracy by the Fourier transform of the phase  $\Phi(\vec{\rho})$  of the object transmission function (A.8). In this case, the differential intensity is an enhanced phase signal. We can extend the result for a single atom to a thin sample. Under the approximation of independent atoms, the potential of a thin sample can be expressed by summing up the potentials of the constituent atoms:

$$V(\vec{\rho}) = \sum_j V_j(\vec{\rho} - \vec{\rho}_j). \quad (\text{A.11})$$

Here  $\vec{\rho}_j$  denotes the location of the  $j$ th atom. By taking the Fourier transform of the intensity  $I(\vec{\rho})$  of the ADPC image, we obtain the object spectrum  $\tilde{I}(\vec{Q})$ :

$$\tilde{I}(\vec{Q}) = \sum_j \tilde{I}_j(\vec{Q}) e^{-i\vec{\rho}_j \cdot \vec{Q}}. \quad (\text{A.12})$$

Here  $\tilde{I}_j(\vec{Q})$  is the Fourier transform of the ADPC image for the  $j$ th atom.

## Appendix B. Material-free phase plates formed by the adjustable aberrations of the correctors

The ideal Fresnel phase plate utilized by the ADPC mode must satisfy the requirements:

1. The phase shift of the even zones is zero while that of the odd zone is  $-\pi/2$ , as depicted in Fig. 1;
2. The total area of the even zones equals that of the odd zones.

The ideal Fresnel phase plate can be approximated with a sufficient degree of accuracy by adjusting the aberration coefficients of the corrector. The number of adjustable zones  $(n+3)/2$  depends on the order  $n$  ( $n=3, 5, \dots$ ) of the lowest order of the spherical aberration which cannot be adjusted. In the case of  $C_3$ -correction, four zones can be obtained; and in the case of  $C_5$ -correction, five zones can be obtained.

The phase shift  $\chi(q)$  of the probe function  $e^{i\chi(q)}$  is given by

$$\chi(q) = -\pi(C_1\lambda q^2 + \frac{1}{2}C_3\lambda^3 q^4 + \frac{1}{3}C_5\lambda^5 q^6 + \frac{1}{4}C_7\lambda^7 q^8 + \dots). \quad (\text{B.1})$$

Based on the phase requirements, the aberration coefficients and the boundary angle  $\theta_m$  are given in Table 1 for the ADPC mode of a  $C_c/C_3$ -corrected STEM and of a  $C_c/C_5$ -corrected STEM, respectively.

## Appendix C. Optimal aberration parameters for IBF and HAADF imaging

The optimal phase shift of the probe for IBF and HAADF imaging is derived based on the condition:

$$\int |\chi(\vec{q}) \pm \frac{\pi}{2}| d\vec{q} \rightarrow \min. \quad (\text{C.1})$$

Here  $\chi$  has the form in (B.1). The sign ‘+’ represents the bright-atom imaging condition and ‘−’ represents the dark-atom imaging condition.

The aberration coefficients for bright-atom imaging have been obtained by using the least-square approach. The results for positive  $C_5$  in the case of the  $C_c/C_3$ -corrected microscope and for positive  $C_7$  in the case of the  $C_c/C_5$ -corrected microscope are listed in Table 2.

## References

- [1] C. Ophus, J. Ciston, J. Pierce, T.R. Harvey, J. Chess, B.J. McMorran, C. Czarnik, H.H. Rose, P. Ercius, Efficient linear phase contrast in scanning transmission electron microscopy with matched illumination and detector interferometry, Nat. Commun. 7 (2016) 10719.
- [2] H. Rose, Phase contrast in scanning transmission electron microscopy, Optik 39 (4) (1974) 416–436.
- [3] N. Dekkers, H. De Lang, Differential phase contrast in a STEM, Optik 41 (4) (1974)



- 452–456.
- [4] H. Rose, Nonstandard imaging methods in electron microscopy, *Ultramicroscopy* 2 (1977) 251–267.
  - [5] M. Linck, P. Hartel, S. Uhlemann, F. Kahl, H. Müller, J. Zach, M. Haider, M. Niestadt, M. Bischoff, J. Biskupek, et al., Chromatic aberration correction for atomic resolution TEM imaging from 20 to 80 kv, *Phys. Rev. Lett.* 117 (7) (2016) 076101.
  - [6] I. Lazić, E.G. Bosch, S. Lazar, Phase contrast STEM for thin samples: integrated differential phase contrast, *Ultramicroscopy* 160 (2016) 265–280.
  - [7] J. Chapman, R. Ploessl, D. Donnet, Differential phase contrast microscopy of magnetic materials, *Ultramicroscopy* 47 (4) (1992) 331–338.
  - [8] S. Majert, H. Kohl, High-resolution STEM imaging with a quadrant detector – conditions for differential phase contrast microscopy in the weak phase object approximation, *Ultramicroscopy* 148 (2015) 81–86.
  - [9] M. Haider, A. Epstein, P. Jarron, C. Boulon, A versatile, software configurable multichannel STEM detector for angle-resolved imaging, *Ultramicroscopy* 54 (1) (1994) 41–59.
  - [10] S. Lopatin, Y.P. Ivanov, J. Kosel, A. Chuvilin, Multiscale differential phase contrast analysis with a unitary detector, *Ultramicroscopy* 162 (2016) 74–81.
  - [11] T.J. Pennycook, A.R. Lupini, H. Yang, M.F. Murfitt, L. Jones, P.D. Nellist, Efficient phase contrast imaging in STEM using a pixelated detector. part 1: experimental demonstration at atomic resolution, *Ultramicroscopy* 151 (2015) 160–167.
  - [12] H. Yang, T.J. Pennycook, P.D. Nellist, Efficient phase contrast imaging in STEM using a pixelated detector. part II: optimisation of imaging conditions, *Ultramicroscopy* 151 (2015) 232–239.
  - [13] M. Krajnak, D. McGrouther, D. Maneuski, V. O'Shea, S. McVitie, Pixelated detectors and improved efficiency for magnetic imaging in STEM differential phase contrast, *Ultramicroscopy* 165 (2016) 42–50.
  - [14] R. Close, Z. Chen, N. Shibata, S. Findlay, Towards quantitative, atomic-resolution reconstruction of the electrostatic potential via differential phase contrast using electrons, *Ultramicroscopy* 159 (2015) 124–137.
  - [15] J. Chapman, P. Batson, E. Waddell, R. Ferrier, The direct determination of magnetic domain wall profiles by differential phase contrast electron microscopy, *Ultramicroscopy* 3 (1978) 203–214.
  - [16] M. Lohr, R. Schregle, M. Jetter, C. Wächter, T. Wunderer, F. Scholz, J. Zweck, Differential phase contrast 2.0 – Opening new fields for an established technique, *Ultramicroscopy* 117 (2012) 7–14.
  - [17] N. Shibata, S.D. Findlay, Y. Kohno, H. Sawada, Y. Kondo, Y. Ikuhara, Differential phase-contrast microscopy at atomic resolution, *Nat. Phys.* 8 (8) (2012) 611–615.
  - [18] K. Müller, F.F. Krause, A. Béché, M. Schowalter, V. Galioit, S. Löffler, J. Verbeeck, J. Zweck, P. Schattschneider, A. Rosenauer, Atomic electric fields revealed by a quantum mechanical approach to electron picodiffraction, *Nat. Commun.* 5 (2014) 5653.
  - [19] B. Bauer, J. Hubmann, M. Lohr, E. Reiger, D. Bougeard, J. Zweck, Direct detection of spontaneous polarization in wurtzite GaAs nanowires, *Appl. Phys. Lett.* 104 (21) (2014) 211902.
  - [20] A. Lubk, J. Zweck, Differential phase contrast: an integral perspective, *Phys. Rev. A* 91 (2) (2015) 023805.
  - [21] U. Kaiser, J. Biskupek, J. Meyer, J. Leschner, L. Lechner, H. Rose, M. Stöger-Pollach, A. Khlobystov, P. Hartel, H. Müller, et al., Transmission electron microscopy at 20 kv for imaging and spectroscopy, *Ultramicroscopy* 111 (8) (2011) 1239–1246.
  - [22] S. Uhlemann, H. Müller, P. Hartel, J. Zach, M. Haider, Thermal magnetic field noise limits resolution in transmission electron microscopy, *Phys. Rev. Lett.* 111 (4) (2013) 046101.
  - [23] M. Haider, P. Hartel, H. Müller, S. Uhlemann, J. Zach, Information transfer in a TEM corrected for spherical and chromatic aberration, *Microsc. Microanal.* 16 (04) (2010) 393–408.